1 **Visualizing cellular and tissue ultrastructure using Ten-fold Robust Expansion Microscopy**

2 **(TREx)**

3 Hugo G.J. Damstra[1], Boaz Mohar[2], Mark Eddison[2], Anna Akhmanova[1], Lukas C. Kapitein[1*], Paul W.

4 Tillberg[2*]

5 [1]Cell Biology, Neurobiology and Biophysics, Department of Biology, Faculty of Science, Utrecht

6 University, Utrecht, The Netherlands

7 [2]Janelia Research Campus, HHMI, Ashburn, Virginia 20147, USA

8 Correspondence: l.kapitein@uu.nl; tillbergp@janelia.hhmi.org

9   **ABSTRACT**

10   Expansion microscopy (ExM) is a powerful technique to overcome the diffraction limit of light microscopy

11   that can be applied in both tissues and cells. In ExM, samples are embedded in a swellable polymer gel to

12   physically expand the sample and isotropically increase resolution in x, y and z. The maximum resolution

13   increase is limited by the expansion factor of the polymer gel, which is four-fold for the original ExM

14   protocol. Variations on the original ExM method have been reported that allow for greater expansion

15   factors, for example using iterative expansion, but at the cost of ease of adoption or versatility. Here, we

16   systematically explore the ExM recipe space and present a novel method termed Ten-fold Robust

17   Expansion Microscopy (TREx) that, like the original ExM method, requires no specialized equipment or

18   procedures to carry out. We demonstrate that TREx gels expand ten-fold, can be handled easily, and can be

19   applied to both thick tissue sections and cells enabling high-resolution subcellular imaging in a single

20   expansion step. We show that applying TREx on antibody-stained samples can be combined with off-the-

21   shelf small molecule stains for both total protein and membranes to provide ultrastructural context to

22   subcellular protein localization.

23 **INTRODUCTION**

24 Expansion Microscopy (ExM) circumvents the diffraction limit of light microscopy by physically

25 expanding the specimen four-fold in each dimension (Chen, Tillberg and Boyden, 2015; Tillberg *et al.*,

26 2016). While other super-resolution approaches require specialized optics (Hell and Wichmann, 1994),

27 fluorophores (Rust, Bates and Zhuang, 2006), or software (Gustafsson, 2000), and are not readily

28 compatible with thick tissue slices, ExM is compatible with any microscope (Zhang *et al.*, 2016; Gao *et al.*,

29 2019), including combinations with other super resolution modalities (Halpern *et al.*, 2017; Gao *et al.*,

30 2018; Xu *et al.*, 2019), and performs well in both cultured cells and thick tissue slices (Chen, Tillberg and

31 Boyden, 2015; Tillberg *et al.*, 2016). The resolution increase of ExM depends on labeling efficiency,

32 anchoring efficiency, and the expansion factor of the gel recipe used. Recently, method variants have been

33 described that increase the expansion factor to increase the maximum resolution obtainable with ExM. For

34 example, iterative ExM (iExM) uses sequential embedding in multiple expansion gels to achieve 15x and

35 greater expansion but requires a complex sequence of gel re-embedding, link cleaving, and fluorophore

36 transfer (Chang *et al.*, 2017), limiting broad adoption in biological labs.

37 The expansion factor of the gel itself can be increased by decreasing the concentration of

38 crosslinker (Okay, 2009), usually bisacrylamide (bis), at the expense of gel mechanical integrity. For

39 example, reducing the bis in the original ExM recipe from 1.5 ppt (parts per thousand) to 250 ppm (parts

40 per million) produces a ~9x expanding gel (Chen, Tillberg and Boyden, 2015, SF5), but these gels are too

41 soft to hold their shape under the force of gravity. As a result, they are difficult to handle without breaking

42 and display non-uniform expansion. This tradeoff of expansion versus gel mechanical integrity has not been

43 explored in a quantitative or systematic way.

44 Another gel recipe variant, using a high concentration of the monomer dimethylacrylamide

45 (DMAA), has enough crosslinking through side reactions and polymer chain entanglement that the

46 crosslinker can be omitted entirely, producing ~10-fold expansion in one step (Truckenbrodt *et al.*, 2018).

47 This recipe has been used to expand cultured cells and thin cryosectioned tissue (Truckenbrodt *et al.*, 2019),

48 but this recipe reportedly requires rigorous degassing to remove oxygen prior to gelation, making it

49 laborious to adopt. Moreover, expansion of >50 μm thick tissue slices has not been demonstrated using this

50 method. Thus, a robustly validated and easily adoptable method that is compatible with multiple sample

51 types and enables single step expansion well over 4x without compromising gel integrity is lacking.

52 Here, we explored the expansion gel recipe space in a systematic manner, assessing the limits of

53 single-round expansion using reagents and methods that would be familiar to labs already doing standard

54 ExM. For any given choice of recipe parameters (monomer concentrations, gelation temperature, radical

3

55   initiation rate, etc.), varying the crosslinker alone yielded a family of recipes whose expansion factor and

56   mechanical quality vary smoothly from high expanding, poor quality to low expanding, excellent quality

57   gels. A range of crosslinker concentrations was tested because the optimal crosslinker concentration may

58   be different for each recipe family. Here we present an optimized ExM method that allows for robust ten-

59   fold expansion in a single step, termed TREx. We show TREx can be used to expand thick tissue slices and

60   adherent cells and is compatible with antibodies, as well as off-the-shelf small molecule stains for total

61   protein and membranes. Together, we show how TREx enables 3D nanoscopic imaging of specific

62   structures stained with antibodies in combination with cellular ultrastructure.

63   **RESULTS**

64   To systematically explore the expansion recipe space, we developed a streamlined method for

65   synthesizing dozens of gel recipes and characterizing their mechanical quality in parallel. For every set of

66   gel recipe parameters (component concentrations and gelation temperature, listed in Fig. 1A) we define a

67   recipe family as the set of recipes generated by varying the crosslinker (bisacrylamide) concentration. For

68   each family, we tested five recipes with crosslinker concentrations log-spaced from 1 ppt (parts per

69   thousand or mg/mL) to 10 ppm (parts per million), plus one with zero crosslinker. We also included the

70   original ExM recipe, with 1.5 ppt crosslinker. For each recipe, we cast three gel specimens, expanded them

71   fully in water, and measured the expansion factor (Fig. 1B). We found that resistance to deformation under

72   the force of gravity was a good proxy for the more subjective judgement of ease of gel handling. We

73   measured gel deformation by placing a semicircular punch from each gel upright on its curved edge and

74   allowing the gel corners to deflect under the force of gravity. We defined the deformation index as the

75   vertical displacement of each gel corner, divided by the gel radius (Fig. 1C), which ranges from 0 (for gels

76   that do not deform) to 1 (for gels that deform freely under their own weight). We manually calibrated this

77   measurement, finding that deformation indices between 0 and 0.125 corresponded to gels with excellent

78   ease of handling, 0.125 to 0.25 corresponded to acceptable ease of handling, and anything higher than 0.25

79   was unacceptable. While not as theoretically informative as elastic modulus and yield strength

80   measurements, this measurement can be repeated and extended to new gel recipes by any lab developing

81   expansion methods, without access to specialized equipment. We plotted the deformation index for each

82   gel as a function of its expansion factor (Fig. 1D).

83   **Development of the TRex gel recipe**

84   We began by characterizing a recipe family generated from the original ExM recipe (family A).

85   Consistent with (Chen, Tillberg and Boyden, 2015), reducing the crosslinker to 300 ppm increased the

86   expansion to ~9x, below which the gels fail to form consistently (Fig. 1B, purple). We next characterized a

4

87   high-monomer recipe family adapted from the 4x-expanding Ultra-ExM recipe (Gambarotto *et al.*, 2019)

88   (family B). Gambarotto et al found that a higher monomer concentration relative to the original ExM recipe

89   was necessary for high fidelity preservation of the shape of centrioles. This was offset with a lower

90   crosslinker concentration of 1 ppt bisacrylamide to achieve 4x expansion. Indeed, for this high-monomer

91   family of recipes, expansion as a function of crosslinker concentration was shifted leftward compared to

92   standard ExM (Fig. 1B, blue). As the crosslinker was decreased below 30 ppm the increase in expansion

93   factor saturated around 11.5x. The deformation index versus expansion factor curve for the high monomer

94   family ran below that for standard ExM, indicating that for a given expansion factor a high-monomer gel

95   holds its shape better than the corresponding standard ExM gel (Fig. 1D, blue).

96   Compared with standard ExM, this high monomer family uses a higher concentration of radical

97   initiator and accelerator to trigger polymerization (5 ppt each of APS and TEMED, versus 2 ppt in standard

98   ExM), which causes gels to form within minutes at room temperature. Because the rates of initiation and

99   polymerization increase with temperature, it is likely that specimens are not fully equilibrating to the

100   gelation temperature of 37 °C before the onset of gelation, introducing a potential source of experimental

101   variability. This rapid gelation makes the gelation chamber assembly step more time sensitive and presents

102   challenges for adapting the technique to thick tissue slices, as thick tissue slices require extra time for the

103   gelation solution to diffuse throughout the sample prior to polymerization. We tested the same high

104   monomer recipe family but with initiator reduced to 1.5 ppt (family C). For all families, the accelerator

105   (TEMED) was varied in tandem with the initiator. The expansion versus crosslinker curve for this family

106   was similar to family B for high crosslinker concentrations but displayed a slightly greater slope. Unlike

107   family B, the expansion factor did not saturate upon decreasing the crosslinker concentration. Instead, the

108   expansion factor continued to increase to 13x expansion at 10ppm crosslinker (Fig. 1B, red), with gels

109   failing to form without any crosslinker present. While deformation of these gels for the same expansion

110   factor was increased compared to family B, although better than for family A and acceptable up to an

111   expansion factor of 10 (30 ppm bis, Fig. 1D, red), in our judgement this was outweighed by the slower and

112   more controlled gelation kinetics achieved by lowering the concentration of initiator and accelerator.

113   The recipe families explored above (B, C) feature a high fraction of sodium acrylate relative to

114   acrylamide. Acrylate drives expansion of the gel but comes in widely varying purity levels and, we found

115   in some cases, causes tissue to shrink. The tissue shrinkage was modest compared to the gel expansion but

116   may not be uniform at all scales. We therefore tested an alternative recipe family (D) with higher acrylamide

117   to acrylate ratio (2.1:1). Increasing the acrylamide to acrylate ratio did not change the expansion factors

118   appreciably at a given crosslinker concentration, suggesting that the swelling effect of acrylate saturates at

5

119   high concentrations. At the maximum expansion factor of ~10, the deformation behavior was comparable

120   to family C, which biased our choice to family D due to the lower acrylate content of the gels.

121   We further tested an elevated gelation temperature of 50 °C (family E), in an attempt to increase

122   the initiation rate without introducing premature gelation at room temperature seen in recipe family B.

123   Compared to family D, the expansion factors were around 15% higher at 100 ppm (6x) and 300 ppm

124   crosslinker (9x), but gelation failed at lower concentrations, leaving family D as the family with a higher

125   maximum expansion factor (i.e., 10x at 30 ppm bis). The deformation versus expansion curve for family E

126   was similar to the other high monomer recipe families (Fig. 1D, green), but was found to be sensitive to

127   processing details, such as the gelation chamber construction and placement within the incubator. This

128   suggests that premature gelation prior to equilibrating at the higher temperature reduces the replicability of

129   this recipe family.

130   Considering all 5 recipe families, family B (high acrylate and high APS/TEMED) displayed the

131   best mechanical performance, i.e. the lowest deformation index for any given expansion factor. Family D

132   (high acrylamide and low APS/TEMED) displayed similar performance, with the deformation index

133   remaining well within the acceptable range for expansion factors up to 10. In handling high-expanding

134   (>8x) gels from all recipe families, we found that while those from the standard ExM family (A) were

135   extremely prone to breaking, those from any of the high monomer families could be handled more easily

136   (and even dropped from a height of several feet) without breaking. Because the reduced initiator

137   concentration of family D results in a slower and more controlled polymerization rate, and because we

138   preferred a lower acrylate content, we chose this recipe family to proceed to biological specimen expansion.

139   We found that the exact expansion factor varied for different gelation chamber geometries but could readily

140   be adjust by finetuning the crosslinker concentration (e.g., 50 ppm for Ashburn, VA, USA experiments

141   versus 90 ppm for Utrecht, The Netherlands experiments), We thus recommend that users test gels with a

142   range of crosslinker concentrations between 30 and 100 ppm to find a suitable recipe for their specimen

143   preparation. We name the resulting method Ten-fold Robust Expansion (TREx) microscopy.

144   **Subcellular imaging of specific proteins and cellular ultrastructure in thick brain slices**

145   A major advantage of ExM over other super-resolution techniques is its compatibility with thick

146   tissue slices. Tissue slices require the onset of gelation to be delayed, usually with low temperature

147   incubation and a radical inhibitor (e.g. 4-Hydroxy-TEMPO; 4HT), to give the monomer solution time to

148   diffuse into the tissue (Chen, Tillberg and Boyden, 2015; Tillberg *et al.*, 2016) . For TREx, we found that

149   in some conditions room oxygen was sufficient to inhibit gelation with shaking on ice indefinitely. To

150   increase robustness for thick tissue slices, we included 15 ppm 4HT, allowing ample time to mount

6

151   specimens in gelation chambers at room temperature. ExM enables uniform expansion by treating
152   embedded tissue with strong proteolytic digestion step. Proteins (including antibodies) are crosslinked to
153   the gel with acryloyl-X SE (AcX), allowing for retention of protein fragments after digestion. Replacing
154   proteolytic digestion with a high detergent, high temperature disruption step has been shown to enable
155   expansion with better overall retention of proteins (Ku *et al.*, 2016; Tillberg *et al.*, 2016; Gambarotto *et al.*,
156   2019; Zwettler *et al.*, 2020). We found that this gentler disruption approach also allowed the AcX anchor
157   treatment to be reduced from 100 µg/mL overnight (standard ExM) to 10 µg/mL for 1 hour while enabling
158   full expansion of mouse brain slices without the appearance of crack-like artifacts.

159   In electron microscopy, non-specific stains for proteins and membranes are commonly used to
160   provide structural detail at high spatial resolution. Recently, the use of non-specific NHS ester protein stains
161   and other small molecule probes has been combined with ExM (M'Saad and Bewersdorf, 2020; Mao *et al.*,
162   2020; Yu *et al.*, 2020). Expansion allows visualization of intracellular detail in densely stained samples,
163   which would not otherwise lead to meaningful contrast. These applications have the promise to bring
164   together the advantages of light microscopy (specific staining using antibodies and volumetric imaging)
165   with the advantage of seeing cellular context typically provided by electron microscopy. Because TREx
166   reaches single-step expansion factors at which small-molecule stains are expected to be useful, we set out
167   to explore this idea further. We applied NHS ester dyes to demonstrate total protein content in thick slices
168   (100 µm) of mouse brain cortex expanded with TREx (Fig. 2A and Supp. Movie 1). The neuropil region
169   outside the cell somas contained a rich profusion of fibers and structures visible in sharp relief. The nucleus
170   of each cell was easily identified, with especially strong staining in nucleoli-like structures. Surrounding
171   each nucleus, the nuclear envelope could be identified, with particularly dense total protein stain on the side
172   facing the nucleus. The nuclear envelope was punctuated by heavily stained spots that span the envelope,
173   consistent with nuclear pore complexes (Fig. 2A, inset). Within the cytosol, several organelles were
174   visualized by either heavy inner staining with a dim border or weak inner staining.

175   We next tested whether antibodies delivered using a standard immunofluorescence procedure
176   before embedding were also retained in the TREx gel. We stained mouse brain cortex tissue for Bassoon (a
177   marker for both excitatory and inhibitory pre-synaptic active zones), Homer (a marker for the excitatory
178   post-synaptic apparatus), and VGAT (a vesicular GABA transporter in the pre-synaptic compartments of
179   inhibitory synapses). After staining and anchoring with AcX, tissue was expanded with TREx and imaged
180   by light sheet microscopy. Numerous putative excitatory synapses were observed at high density, with
181   clearly separated Bassoon and Homer pre- and post-synaptic staining (Fig. 2B and Supp. Movie 2). VGAT
182   had a more extended staining pattern, consistent with the known distribution of synaptic vesicles throughout
183   pre-synaptic boutons. Elaborately shaped compartments with dense VGAT staining were seen with multiple

7

184   synaptic release sites marked by Bassoon (Fig. 2B, inset). As expected, these release sites were not paired

185   with the post-synaptic marker Homer. These results demonstrate the ability of TREx to preserve correct

186   synaptic staining while enabling sub-diffraction limited imaging of large tissue sections.

187   **Subcellular imaging of specific proteins and cellular ultrastructure in cultured cells**

188   We next explored the use of TREx for high-resolution imaging of specific proteins, NHS stains and

189   lipid membranes in cultured cells. For membranes, a custom-synthesized membrane probe compatible with

190   the ExM process has been shown to visualize membrane surfaces in fixed brain tissue (Karagiannis *et al.*,

191   2019). This probe relies on a peptide-modified lipid tail that intercalates in target membranes and provides

192   opportunities for anchoring to the gel through D-lysines its peptide sequence. We asked whether the

193   commercially available membrane-binding fluorophore-cysteine-lysine-palmitoyl group (mCLING) could

194   also be used for membrane staining and gel anchoring. mCLING has been developed as a fixable

195   endocytosis marker consisting of a fluorophore and a short polypeptide group with one cysteine and seven

196   lysines coupled to a palmitoyl membrane anchor (Revelo and Rizzoli, 2016). Due to the presence of

197   multiple lysines, we hypothesized that mCLING would be compatible with standard ExM anchoring

198   through AcX.

199   While the standard protocol for mCLING delivery relies on active endocytosis in living cells, we

200   asked if mCLING would stain intracellular membranes more uniformly when added to fixed cells, which

201   would have the added benefit of not perturbing intracellular membrane trafficking by long incubation in

202   live cells. To test this, we fixed activated Jurkat T cells, incubated the fixed cells with mCLING overnight,

203   and proceeded with the TREx protocol. We found that mCLING efficiently intercalates in both the plasma

204   membrane and internal organelles and is retained following standard AcX treatment (Fig. 3A and Supp.

205   Movie 3).

206   By carefully rendering the imaged volumes we could, with one probe, both appreciate the ruffled

207   morphology of the plasma membrane on top of the flattened part of the cell, and visualize the organelle

208   clustering typical of activated T-cells (Fig. 3A, B). In electron microscopy, distinct morphologies are used

209   to identify organelles. Similarly, we found that we could clearly identify different organelles based on

210   mCLING, suggesting that it could be used for automated segmentation of organelles. Indeed, we found that

211   mitochondria could be readily segmented using a trainable Weka segmentation algorithm (Fig. 3B)

212   (Arganda-Carreras *et al.*, 2017). While the resolution of subcellular structures is limited by the density of

213   mCLING moieties in the membrane, the efficiency of crosslinking to the gel, and the maximum expansion

214   factor, we found TREx allows sufficient single-step expansion to resolve individual mitochondrial cristae,

215   which are known from electron microscopy to be spaced 70 nm apart (Fig. 3C). Although mCLING is

216   thought to be membrane impermeable (due to multiple positively charged amino groups), it readily stained

217   fixed and unpermeabilized cells following extended incubation. Because this approach does not require

218   labeling live cells and is expected to reduce differences in uptake efficiency between intracellular

219   compartments, we used this approach in all subsequent experiments.

220   We next tested if mCLING could also be used to visualize membranes in more complex cell types.

221   To test this, we used differentiated Caco-2 cells grown to form an epithelial monolayer. Using TREx, we

222   could expand the entire monolayer and visualize the membrane using mCLING (Fig. 3D-G and Supp.

223   Movie 4). This enabled us to resolve individual microvilli as hollow membrane protrusions within the dense

224   brush border. In addition, we were able to resolve the elaborate interdigitated cell-cell junctions that could

225   previously only be clearly appreciated using electron microscopy (Drenckhahn and Franz, 1986). The

226   advantage of optical, volumetric imaging is underscored by the fact that we can easily render one dataset

227   in several ways, either resembling scanning electron microscopy to highlight volumetric surface

228   morphology (Fig. 3D), or transmission electron microscopy to explore single planes in more detail (Fig.

229   3E). Together, these data illustrate that TREx can be combined with a commercially available membrane

230   stain to provide rapid volumetric insights into the elaborate membranous architecture of cells.

231   We further tested whether TREx using general membrane stains could be combined with general

232   protein stains and/or antibody stains. U2OS cells transfected with GFP-Sec61β were fixed, treated with

233   mCLING, stained for GFP, and expanded with TREx followed by the NHS stain (Fig. 4A). Because we

234   performed the NHS stain after disruption, we used temperature- and detergent-mediated disruption, rather

235   than proteolytic digestion. We found that secondary antibodies that had been used to stain GFP before

236   gelation withstood this disruption step. We observed a clear degree of overlap between mCLING and NHS,

237   especially in the dense perinuclear region, but we could also identify distinct features of each stain (Fig.

238   4A). Interestingly, we observed strong nucleoplasmic staining in the NHS stain and clear puncta where the

239   imaging plane intersected the nuclear envelope, which presumably are nuclear pores (Fig. 4A). These

240   results demonstrate that general stains for membranes and proteins can be combined with antibody-based

241   labeling to reveal specific proteins in their ultrastructural context.

242   Previously, we have used ExM to study the three-dimensional organization of microtubules (MT)

243   in neurons and T cells (Hooikaas *et al.*, 2020; Jurriens *et al.*, 2020). For high-resolution imaging of the MT

244   cytoskeleton, cells are usually pre-extracted with detergent and glutaraldehyde to remove the soluble pool

245   of tubulin, followed by paraformaldehyde fixation (Tas *et al.*, 2017). This reduces background but does not

246   preserve membranes. We reasoned that the increased expansion of TREx would dilute the background due

247   to soluble tubulin by the expansion factor cubed. Ten-fold expanded microtubules remain diffraction

248   limited in width (i.e., 250-350 nm), so their signal should be reduced only by the expansion factor itself

9

249   (due to the expansion along their length). Therefore, we wondered whether the resulting relative boost in

250   signal over background would eliminate the need for pre-extraction to enable high-resolution imaging of

251   microtubules in combination with membranes. To test this, we fixed cells expressing GFP-Sec61β without

252   pre-extraction, treated them with mCLING, stained for GFP and tubulin, and then proceeded with TREx

253   (Fig. 4B and Supp. Movie 5). Subsequent confocal microscopy revealed the interplay between microtubules

254   and ER in three dimensions and revealed how other membranous organelles were connected to both

255   structures (Fig. 4C). Thus, TREx facilitates high-resolution three-dimensional mapping of specific

256   cytoskeletal and membranous structures in combination with markers that provide ultrastructural context.

257   **DISCUSSION**

258   We developed Ten-fold Robust Expansion (TREx) in order to expand biological specimens 10-fold

259   in a single round of expansion, without specialized equipment or procedures. In developing this method,

260   we established a framework for assessing gel recipes operating near this apparent limit of single-round

261   expansion. We found that the mechanical performance of gel recipes, i.e. resistance to deformation versus

262   gel expansion factor, varies smoothly with changes in crosslinker. For all high monomer (~3 M total

263   acrylamide and acrylate) gel recipe families, the relation between expansion factor and crosslinker

264   concentration fell close to a common curve. The high radical initiation rate of family B enabled gelation

265   without the inclusion of a crosslinker, suggesting that side reactions and polymer entanglement in these

266   conditions create sufficient effective crosslinks to form a gel. Gel deformation measurements versus

267   expansion factor, though less precise, also show high monomer recipe families falling close to a common

268   curve. Compared to the high monomer families, the original ExM recipe family is less resistant to

269   deformation for a given expansion factor and expands more for a given crosslinker concentration. The factor

270   determining gel properties is not crosslinker concentration in the gel recipe *per se*, but rather the density of

271   effective crosslinks formed between neighboring polymer chains in the gel. This suggests that the original,

272   monomer poor recipe less efficiently incorporates crosslinker molecules as effective polymer crosslinks.

273   This may be because the resulting lower rate of chain extension allows incorporated crosslinker molecules

274   to be re-reacted by the same polymer chain before they can react with neighboring polymers.

275   While the expansion factor of the original ExM recipe can be tuned by varying the crosslinker

276   concentration, it has been shown that increasing the monomer content is required to maintain nanoscale

277   isotropy, using centrioles as a convenient standard reference structure (Gambarotto *et al.*, 2019).

278   Considering gel quality versus expansion factor alone, the high monomer recipe family B derived from the

279   U-ExM recipe allows for a 10-fold expanding gel (at crosslinker concentration of 30 ppm) with a low

280   deformation index of 0.13. However, the high radical initiation rate used in this family (5 ppt APS and

281   TEMED) results in fast gelation. This increases the time sensitivity of mounting the specimen in the gelation

10

282   chamber and adds an additional challenge for adapting the method to thick tissues requiring extended

283   incubation in the gelation solution. Recipe families C and D solve this problem by reducing initiation rates,

284   at a slight expense of mechanical performance compared with family B. Like family B, family C has a high

285   acrylate content, which might contribute to imaging artifacts due to shrinkage of the sample prior to gelation

286   and inconsistent acrylate purity. Family D reduces the acrylate content by half while retaining similar

287   mechanical performance to family C, especially in the ten-fold expansion regime. Finally, with family E

288   we explored whether increasing the gelation temperature to 50ºC would produce the improved mechanical

289   performance of family B (through increased temperature-dependent radical initiation) without premature

290   gelation at room temperature. However, we found that this reduced the expansion factor and increased

291   susceptibility to experimental variation. Therefore, we based our TREx recipe on recipe family D. The

292   exact crosslinker concentration that produces 10-fold expanding gels was found to vary between labs (i.e.

293   50 ppm in Ashburn, VA, USA versus 90 ppm in Utrecht, The Netherlands, possibly due to differences in

294   gelation chamber design), so we recommend that each lab test a range of crosslinker concentrations between

295   30 and 100ppm using their choice of specimen, gelation chamber, and incubator.

296   We applied TREx to mouse brain tissue slices stained either for specific targets with antibodies, or for total

297   protein distribution with NHS ester dyes. Single round ten-fold expansion with TREx followed by total

298   protein staining was sufficient to reveal densely packed axons and dendrites running through the neuropil,

299   while individual organelles could be resolved within the neuronal soma. The nuclear envelope, along with

300   presumptive nuclear pore complexes, was also clearly resolved. The correct relative localizations of pre-

301   and post-synaptic markers and pre-synaptic neurotransmitter vesicles stained with standard

302   immunohistochemistry were also retained in TREx-expanded tissue slices.

303   We further demonstrated the utility of TREx for the study of cell biology through combinations

304   with several staining modalities in cultured cells, prepared in several culture formats. After a single round

305   of expansion with TREx, the commercially available membrane stain mCLING was able to clearly resolve

306   the internal structure of mitochondria and the detailed pattern of plasma membrane ruffling in activated

307   Jurkat T cells. While these structures would be readily resolved with electron microscopy, we were able to

308   do so in the context of complete cells, enabling concomitant detection and automated segmentation of

309   mitochondria clustered followed T cell activation. Caco-2 cells grown on permeable filters were also

310   successfully stained with mCLING and expanded with TREx to reveal the detailed structure of epithelial

311   microvilli and membrane interdigitations at the contacts of neighboring cells. These structures had

312   previously been known from electron microscopy but were now imaged with ease in the context of entire

313   cell monolayers. Successful application of TREx to filter-cultured Caco-2 cells further demonstrates the

11

314 robustness of TREx, because we had repeatedly failed to cleanly recover epithelial cultures using standard
315 ExM.

316   Combining mCLING with a total protein stain using NHS esters and an antibody marking the ER
317 in U2OS cells, shows close contacts between ER and other organelles. While the NHS ester and mCLING
318 staining patterns were similar in their overall contours, some clear differences in staining patterns were
319 noted, including the presence of presumptive nuclear pore complexes in the NHS ester channel. The strong
320 overlap between NHS ester and mCLING stains was not unexpected, given the reactivity of NHS esters
321 towards both unreacted lysines in the mCLING molecule and antibodies. However, the extent to which
322 NHS ester staining is truly unbiased over all proteins and how it may be modulated by the local environment
323 awaits further exploration.

324   In U2OS cells, TREx retained anti-tubulin antibody stain with high efficiency, maintaining
325 continuous microtubules with high signal-to-noise ratio after 1000-fold volumetric expansion. Combined
326 staining for ER and all membranes revealed close appositions along microtubules, ER and presumptive
327 mitochondria. In unexpanded cells, high quality antibody staining for microtubules requires monomeric
328 tubulin to be removed with a pre-extraction step, which destroys membranes and extracts other proteins.
329 For specimens expanded with TREx, this is not necessary as the monomeric tubulin signal is diluted 1000-
330 fold volumetrically, while the diameter of an expanded microtubule is still below the diffraction limit, so
331 the signal is only diluted by the the 10-fold linear expansion factor. This 1000-fold volumetric dilution is
332 also what enables the use of dense protein stains such as NHS ester dyes, which in unexpanded specimens
333 would be too dense to resolve any meaningful structure.

334   In summary, by systematically exploring the ExM recipe space we established a novel recipe using
335 standard ExM reagents that can be rapidly adopted by other labs. TREx allows for ten-fold expansion of
336 both thick tissue slices and cells in a single expansion step and has applications in tissue and high-resolution
337 subcellular imaging. Importantly, TREx of antibody-stained samples can be combined with off-the-shelf
338 small molecule stains for both membranes and total protein to provide ultrastructural context.

12

343   **REFERENCES**

344   Arganda-Carreras, I. *et al.* (2017) 'Trainable Weka Segmentation: A machine learning tool for

345   microscopy pixel classification', *Bioinformatics*. doi: 10.1093/bioinformatics/btx180.

346   Chang, J.-B. *et al.* (2017) 'Iterative expansion microscopy', *Nature Methods*. Nature Research, 14(6), pp.

347   593–599. doi: 10.1038/nmeth.4261.

348   Chen, F., Tillberg, P. W. and Boyden, E. S. (2015) 'Expansion microscopy', *Science (New York, N.Y.)*,

349   347(6221), pp. 543–548. doi: 10.1126/science.1260088.

350   Drenckhahn, D. and Franz, H. (1986) 'Identification of actin-, α-actinin-, and vinculin-containing plaques

351   at the lateral membrane of epithelial cells', *Journal of Cell Biology*. doi: 10.1083/jcb.102.5.1843.

352   Gambarotto, D. *et al.* (2019) 'Imaging cellular ultrastructures using expansion microscopy (U-ExM)',

353   *Nature Methods*. Nature Publishing Group, 16(1), pp. 71–74. doi: 10.1038/s41592-018-0238-1.

354   Gao, M. *et al.* (2018) 'Expansion Stimulated Emission Depletion Microscopy (ExSTED)'. doi:

355   10.1021/acsnano.8b00776.

356   Gao, R. *et al.* (2019) 'Cortical column and whole-brain imaging with molecular contrast and nanoscale

357   resolution', *Science*. American Association for the Advancement of Science, 363(6424). doi:

358   10.1126/science.aau8302.

359   Gustafsson, M. G. L. (2000) 'Surpassing the lateral resolution limit by a factor of two using structured

360   illumination microscopy', *Journal of Microscopy*. John Wiley & Sons, Ltd, 198(2), pp. 82–87. doi:

361   10.1046/j.1365-2818.2000.00710.x.

362   Halpern, A. R. *et al.* (2017) 'Hybrid Structured Illumination Expansion Microscopy Reveals Microbial

363   Cytoskeleton Organization', *ACS Nano*, 11(12), pp. 12677–12686. doi: 10.1021/acsnano.7b07200.

364   Hell, S. W. and Wichmann, J. (1994) 'Breaking the diffraction resolution limit by stimulated emission:

365   stimulated-emission-depletion fluorescence microscopy', *Optics Letters*. The Optical Society, 19(11), p.

366   780. doi: 10.1364/ol.19.000780.

367   Hooikaas, P. J. *et al.* (2020) 'Kinesin-4 kif21b limits microtubule growth to allow rapid centrosome

13

368   polarization in t cells', *eLife*. eLife Sciences Publications Ltd, 9, pp. 1–75. doi: 10.7554/ELIFE.62876.

369   Jurriens, D. *et al.* (2020) 'Mapping the neuronal cytoskeleton using expansion microscopy', in *Methods in*
370   *Cell Biology*. doi: 10.1016/bs.mcb.2020.04.018.

371   Karagiannis, E. D. *et al.* (2019) 'Expansion Microscopy of Lipid Membranes', *bioRxiv*. doi:
372   10.1101/829903.

373   Ku, T. *et al.* (2016) 'Multiplexed and scalable super-resolution imaging of three-dimensional protein
374   localization in size-adjustable tissues', *Nature Biotechnology*, 34(9), pp. 973–981. doi: 10.1038/nbt.3641.

375   M'Saad, O. and Bewersdorf, J. (2020) 'Light microscopy of proteins in their ultrastructural context',
376   *Nature Communications*. doi: 10.1038/s41467-020-17523-8.

377   Mao, C. *et al.* (2020) 'Feature-rich covalent stains for super-resolution and cleared tissue fluorescence
378   microscopy', *Science Advances*. American Association for the Advancement of Science, 6(22), p.
379   eaba4542. doi: 10.1126/sciadv.aba4542.

380   Okay, O. (2009) 'General Properties of Hydrogels', in Gerlach G., A. K. (ed.) *Hydrogel Sensors and*
381   *Actuators. Springer Series on Chemical Sensors and Biosensors (Methods and Applications)*. vol. 6.
382   Springer, Berlin, Heidelberg, pp. 1–14. doi: 10.1007/978-3-540-75645-3_1.

383   Revelo, N. H. and Rizzoli, S. O. (2016) 'The membrane marker mCLING reveals the molecular
384   composition of trafficking organelles', *Current Protocols in Neuroscience*. doi:
385   10.1002/0471142301.ns0225s74.

386   Rust, M. J., Bates, M. and Zhuang, X. W. (2006) 'Sub-diffraction-limit imaging by stochastic optical
387   reconstruction microscopy (STORM)', *Nat Methods*, 3(10), pp. 793–795. doi: Doi 10.1038/Nmeth929.

388   Tas, R. P. *et al.* (2017) 'Differentiation between Oppositely Oriented Microtubules Controls Polarized
389   Neuronal Transport', *Neuron*. doi: 10.1016/j.neuron.2017.11.018.

390   Tillberg, P. W. *et al.* (2016) 'Protein-retention expansion microscopy of cells and tissues labeled using
391   standard fluorescent proteins and antibodies', *Nature Biotechnology*. Nature Publishing Group, 34(9), pp.
392   987–992. doi: 10.1038/nbt.3625.

393   Truckenbrodt, S. *et al.* (2018) 'X10 expansion microscopy enables 25-nm resolution on conventional
394   microscopes.', *EMBO reports*. EMBO Press, 19(9), p. e45836. doi: 10.15252/embr.201845836.

395   Truckenbrodt, S. *et al.* (2019) 'A practical guide to optimization in X10 expansion microscopy', *Nature*
396   *Protocols*. doi: 10.1038/s41596-018-0117-3.

14

397   Xu, H. *et al.* (2019) 'Molecular organization of mammalian meiotic chromosome axis revealed by

398   expansion STORM microscopy', *Proceedings of the National Academy of Sciences of the United States of*

399   *America*. National Academy of Sciences, 116(37), pp. 18423–18428. doi: 10.1073/pnas.1902440116.

400   Yu, C.-C. (Jay) *et al.* (2020) 'Expansion microscopy of C. elegans', *eLife*, 9. doi: 10.7554/eLife.46249.

401   Zhang, Y. S. *et al.* (2016) 'Hybrid Microscopy: Enabling Inexpensive High-Performance Imaging

402   through Combined Physical and Optical Magnifications', *Scientific Reports*. Nature Publishing Group,

403   6(1), p. 22691. doi: 10.1038/srep22691.

404   Zwettler, F. U. *et al.* (2020) 'Molecular resolution imaging by post-labeling expansion single-molecule

405   localization microscopy (Ex-SMLM)', *bioRxiv*. Cold Spring Harbor Laboratory, p. 2020.03.12.988923.

406   doi: 10.1101/2020.03.12.988923.

407

408 **MATERIAL AND METHODS**

409 **Gelation chambers for recipe space exploration**

410 A glass slide served as the bottom piece of each gelation chamber. Four strips of 250 μm-thick adhesive

411 silicone material (Digikey cat# L37-3F-320-320-0.25-1A), ~3 mm wide and running the width of the slide,

412 were adhered to the slide to partition it into three separate chambers, each ~12 mm wide. A plus-charged

413 glass slide was placed over the silicone strips to form the top of the gelation chamber and held in place with

414 tape. Two sides of each chamber were open to air, providing a convenient fill port for adding ~100 uL of

415 monomer solution after chamber construction.

416 **Gel synthesis and characterization for recipe space exploration**

417 Sodium acrylate was made by neutralizing acrylic acid (Sigma, 147230) by adding NaOH until the pH

418 reached the range of 7.5-8. Initial neutralization (until pH ~7) was done with 10 N NaOH on ice and using

419 a fume hood to avoid acrylic acid vapor. Neutralization was done in a volume of water calculated to yield

420 a final concentration of 4 M sodium acrylate. The gel recipes for each family contained 1xPBS and the

421 amounts of acrylamide (Sigma, A4058), sodium acrylate, and initiator (APS, Sigma, A3678) indicated in

422 Fig. 1A. Each gel recipe contained the same amount of TEMED (Sigma, T7024) as APS. For each recipe

423 family, gelation solution with crosslinker withheld (but including APS and TEMED) was premixed on ice,

424 in one tube for each recipe family. This solution was then split into six tubes and mixed with serial dilutions

425 of crosslinker (bisacrylamide, Sigma, M1533) to arrive at final crosslinker concentrations of 1 ppt, 300,

426 100, 30, and 10 ppm, and 0. Complete gelation solution thus obtained was pipetted into gelation chambers

427 and incubated at 50 ºC for 1 hour or 37 ºC for 2 hours. Gels were then cooled for 15 minutes at room

428 temperature and chamber tops carefully removed. Gels typically remained stuck exclusively to the top (plus

429 charged) slide. Specimens of each gel were taken with a 6 mm biopsy punch, taking care to avoid material

430 within ~2 mm of the chamber edges (due to oxygen exposure during gelation). Excess gel was scrapped

431 away with a razor blade. A few drops of distilled water were pipetted onto each gel to help release them

432 from the glass slide. Each 6 mm gel specimen was gently released from the slide with a razor blade, placed

433 in a 9 cm Petri Dish and expanded by washing with excess water 2x 15 minutes followed by 2x 1 hour.

434 Diameters of expanded gels were measured and divided by 6 mm to obtain the expansion factor. A semi-

435 circle 25 mm in diameter was punched from each gel using a cookie cutter. Semi-circular gel punches were

436 placed in a plastic tray, which was stood up on end so that the gel stood upright on its curved side. For stiff

437 gels, the top edge remained straight and level while for weak gels the top edge deformed under the force of

438 gravity to form a curve. Each gel was photographed, with a ruler positioned for scale. Using image J, each

16

439   top edge was described by seven manually chosen points, which were then fit to a circle. This best-fit circle

440   was used to calculate the vertical deviation of the gel corners, which was divided by the gel radius to obtain

441   the deformation index.

442   **TREx gelation solution**

443   Sodium acrylate was either purchased (Sigma, 408220) or made by neutralizing acrylic acid by adding

444   NaOH until the pH reached the range of 7.5-8. Initial neutralization (until pH ~7) was done with 10N NaOH

445   on ice and using a fume hood to avoid acrylic acid vapor. TREx gelation solution contains 1.1 M sodium

446   acrylate, 2.0 M acrylamide (AA), 50 ppm (for tissue slices prepared at Janelia) or 90ppm (for cultured cells

447   prepared at University of Utrecht) N,N'-methylenebisacrylamide (bis), PBS (1x), 1.5 ppt APS, 1.5 ppt

448   TEMED, and (optionally, for thick tissue slices) 15 ppm 4HT. Monomer solution was made by combining

449   all components of gelation solution except APS, TEMED, and 4HT. Monomer solution may be aliquoted

450   and stored at -20°C, but must be thawed at room temperature and thoroughly vortexed before use to

451   redissolve any acrylamide crystals that may have precipitated at low temperature before freezing. 4HT,

452   TEMED, and APS were added to monomer solution to produce gelation solution directly before use.

453   **Tissue experiments**

454   Mice were transcardially perfused with ice cold 4% formaldehyde in 100 mM sodium phosphate buffer, pH

455   7.4. Brains were dissected out and post-fixed in 4% formaldehyde overnight at 4°C, followed by washing

456   with PBS (1x) and slicing at 100 μm by vibratome. Slices were optionally stained with standard IHC

457   procedures. Primary antibodies (Chicken anti Bassoon Synaptic systems cat#141016, RRID:AB_2661779;

458   Rabbit anti Homer abcam cat#97593, RRID:AB_10681160; Ms IgG3 VGAT SySy cat#131011,

459   RRID:AB_887872) were used at 1:300 dilution in PBS with 0.1% Triton and 2% BSA (PBT) overnight at

460   4°C. Sections were washed 3x 30min in PBT and given at least 6h in secondary antibodies 1:500 in PBT at

461   room temperature (Goat Anti-Rabbit alexa 488 abcam cat#150077, RRID:AB_2630356; Goat anti-Mouse

462   IgG3 alexa 594 invitrogen cat# A-21155, RRID: AB_2535785; Goat anti chicken CF633 biotium

463   cat#20126, RRID: AB_10852831). After 3x 30min washes in PBS, slices were treated with 10 μg/mL AcX

464   in PBS for 1 hour at room temperature, followed by rinsing with PBS. Slices were incubated with TREx

465   gelation solution (using 50ppm bis, and with 4HT added up to 15ppm), for 20min on ice, with shaking.

466   Following incubation on ice, each tissue specimen was placed on a glass slide at room temperature. Four

467   dabs of vacuum grease were applied to the slide, with each dab at least several mm from the tissue specimen.

468   A coverslip was placed over the tissue and vacuum grease dabs, and pressed down until contacting the

469   tissue, taking care not to let the tissue slide around on the slide. The vacuum grease served to hold the

17

470   assembly in place, thus forming the gelation chamber. Gelation solution was pipetted into the chamber from

471   the side to fully surround the tissue. The chamber was incubated at 37 °C for 1 hour to complete gelation.

472   Following embedding, excess gel was removed with a razor blade, and gelled slices were recovered into

473   disruption buffer (5% SDS, 200 mM NaCl, 50 mM Tris pH 7.5), using a razor blade to gently release them

474   from the glass slide. Gels were incubated at 80 °C for 3 hours, followed by washing in water once and PBS

475   several times to remove residual SDS. Slices were optionally stained with BODIPY-FL NHS at 10-20 μM

476   (and optionally DAPI) in PBS for 1 hour at room temperature. Disrupted slices were placed in glass bottom

477   6-well plates and washed in milliQ water 3x 15 minutes followed by 2x 1 hour to fully expand. Gels with

478   total protein stain were imaged by confocal microscopy using a Zeiss LSM 800 with 40x/1.2NA, water

479   immersion objective. Gels with synaptic antibody stains were imaged on a Zeiss Z1 lightsheet microscope

480   with 10x/0.3NA illumination objectives and 20x/1.0NA water immersion detection objective. Scale bar

481   represent the expanded size divided by the approximate expansion factor of 10.

Cell culture and T cell activation

483   Jurkat T cells (clone E6.1) were grown in RPMI 1640 medium w/ L-Glutamine (Lonza) supplemented with

484   9% Fetal Bovine Serum and 1% penicillin/streptomycin. For T cell activation, 18 mm #1.5 coverslips

485   (Marienfeld, 107032) were coated with Poly-D-Lysine (Thermo Fisher Scientific, A3890401), washed with

486   phosphate buffered saline (PBS) and incubated overnight at 4 °C with a mouse monoclonal anti-CD3 (clone

487   UCHT1, StemCell Technologies, #60011) 10 μg/mL in PBS. Cells were spun down for 4 minutes at 1000

488   rpm and resuspended in fresh, prewarmed RPMI 1640 medium, after which cells were incubated on the

489   coated coverslips for 3 minutes prior to fixation. U2OS cells were cultured in DMEM medium

490   supplemented with 9% Fetal Bovine Serum and 1% penicillin/streptomycin. U2OS cells were transfected

491   with GFP-Sec61β (Addgene, 15108) using FuGENE6 (Promega). Caco2-BBE cells (a gift from S.C.D. van

492   IJzendoorn, University Medical Center Groningen, The Netherlands) were maintained in DMEM

493   supplemented with 9% FBS, 50 μg/μl penicillin/streptomycin and 2 mM L-glutamine. For imaging, cells

494   were seeded on 6.5 mm Transwell filters (3470; Corning) at a density of 1 x 10^5/cm^2 and cultured for 10-

495   12 days to allow for spontaneous polarization and brush border formation.

Immunofluorescence, mCLING treatment and antibodies

497   For all experiments, cells were fixed for 10 minutes with pre-warmed (37 °C) 4% paraformaldehyde + 0.1%

498   glutaraldehyde in PBS. For visualization of lipid membranes, cells were washed twice in PBS after fixation

499   and incubated in 5 μM either mCLING-Atto647N (Synaptic Systems, 710 006AT1) or mCLING-Atto488

500   (Fig. 3C, Synaptic Systems, 710 006AT3) in PBS overnight at RT. The following day, cells were fixed a

18

501   second time with pre-warmed (37 °C) 4% paraformaldehyde + 0.1% glutaraldehyde in PBS. Next, cells

502   were washed with PBS and permeabilized using PBS + 0.2% Triton X-100. Epitope blocking and antibody

503   labeling steps were performed in PBS + 3% BSA. For immunofluorescence staining, we used a rabbit

504   monoclonal antibody against α-tubulin (clone EP1332Y, Abcam, ab52866) and a chicken polyclonal

505   antibody against GFP (Aves Labs, GFP-1010) in combination with goat anti-rabbit IgG (H+L) Alexa Fluor

506   594 (Molecular Probes, a11037) and goat anti-chicken IgY (H+L) Alexa Fluor 488 (Molecular Probes,

507   a11039), respectively.

TREx protocol and NHS staining

509   For TREx Microscopy, samples were treated with 0.1 mg/mL acryloyl X-SE (AcX) (Thermo Fisher,

510   A20770) in PBS overnight at RT. TEMED and APS were added to monomer solution (1.5 ppt each) to

511   produce gelation solution. 170 µL of gelation solution was transferred to a silicone mold with inner diameter

512   of 13 mm (Sigma-Aldrich, GBL664107) attached to a parafilm-covered glass slide, with the sample put

513   cell-down on top to close off the gelation chamber. The sample was directly transferred to a 37 °C incubator

514   for 1 hour to fully polymerize the gel. All gels excluding samples that were processed for subsequent NHS

515   ester staining were transferred to a 12-well plate and digested with 7.5 U/mL Proteinase-K (Thermo Fisher,

516   EO0491) in TAE buffer (containing 40 mM Tris, 20 mM acetic acid and 1 mM EDTA) supplemented with

517   0.5% Triton X-100, 0.8 M guanidine-HCl, and DAPI for 4 hours at 37 °C. The gel was transferred to a Petri

518   dish, water was exchanged 2x 30 minutes and the sample was left in milliQ water to expand overnight.

519   For NHS-staining, gels were first treated in disruption buffer containing 200 mM SDS, 200 mM NaCl and

520   50 mM Tris pH 6.8 for 1.5 hours at 78°C. Gels were washed twice for 15 minutes in PBS and incubated

521   with 20 µg/mL Atto 594 NHS ester (Sigma-Aldrich, 08471) in PBS prepared from a 20 mg/mL stock

522   solution in DMSO for 1 hour at RT with shaking. After staining, gels were washed with excess of PBS,

523   transferred to a Petri dish, and expanded overnight. Prior to imaging the cells were trimmed using a scalpel

524   blade to fit in a Attofluor Cell Chamber (Molecular probes A-7816).

Image acquisition and analysis

526   All cultured cell ExM images were acquired using a Leica TCS SP8 STED 3X microscope equipped with

527   a HC PL APO 86x/1.20W motCORR STED (Leica 15506333) water objective. A pulsed white laser (80

528   MHz) was used for excitation. The internal Leica GaAsP HyD hybrid detectors were used with a time gate

529   of $1 \leq tg \leq 6$ ns. The set-up was controlled using LAS X and run without stimulated emission depletion

530   (STED).

19

531   All data processing and analysis was done using ImageJ and Arivis.

532   For Fig. 2A, raw data was drift corrected using Huygens Professional (SVI) and imported into ImageJ
533   where a sum-projection of 2 planes (z-spacing: 0.8 µm) was made. Fig. 2B is a maximum projection of 2
534   planes (z-spacing: 0.38 µm) and indicated zoom is a volumetric render of the raw data in Arivis. For Fig.
535   3A, raw data was imported in Arivis, a Discrete Gaussian Filter with smoothing radius of 2 was applied
536   and this dataset was used for volumetric renders and clipping. Gamma was adjusted manually to increase
537   visibility of plasma membrane ruffles and intracellular organelles in the same view. For Fig. 3B, the same
538   raw dataset was imported in ImageJ and a sum-projection of 3 planes (z-spacing: 0.35 µm) around the plane
539   of the immunological synapse was segmented for mitochondria using the trainable Weka segmentation
540   plugin in ImageJ. Fig. 3C is a sum-projection of 3 planes (z-spacing 0.35 µm). The linescan in Fig. 3C
541   was generated using ImageJ and processed using Graphpad Prism 8.

542   For Fig. 3D, raw data was imported in Arivis, a Discrete Gaussian Filter with smoothing radius of 2 was
543   applied and this dataset was volumetrically rendered with the opacity mapped to the z-axis. For Fig. 3E,
544   raw data was imported in ImageJ and a running sum projection of 5 slices (z-spacing 0.35 µm) was
545   generated using the RunningZProjector plugin and gamma was adjusted manually to increase intracellular
546   contrast. The resulting image was imported into Arivis for volumetric rendering. Fig. 3F and G are
547   maximum projections of 3 planes (z-spacing: 0.35 µm) and respective zooms.

548   Fig 4A is a maximum projection of 3 planes (z-spacing: 0.35 µm). For Fig 4B, raw data was imported into
549   Arivis, a Discrete Gaussian Filter with smoothing radius of 2 was applied and this dataset was used for
550   volumetric renders and clipping. Fig 4C is a sum projection of 3 slices (z-spacing 0.35 µm) of the same raw
551   data as Fig. 4B and was processed using ImageJ.

552

553

554

555

556

20
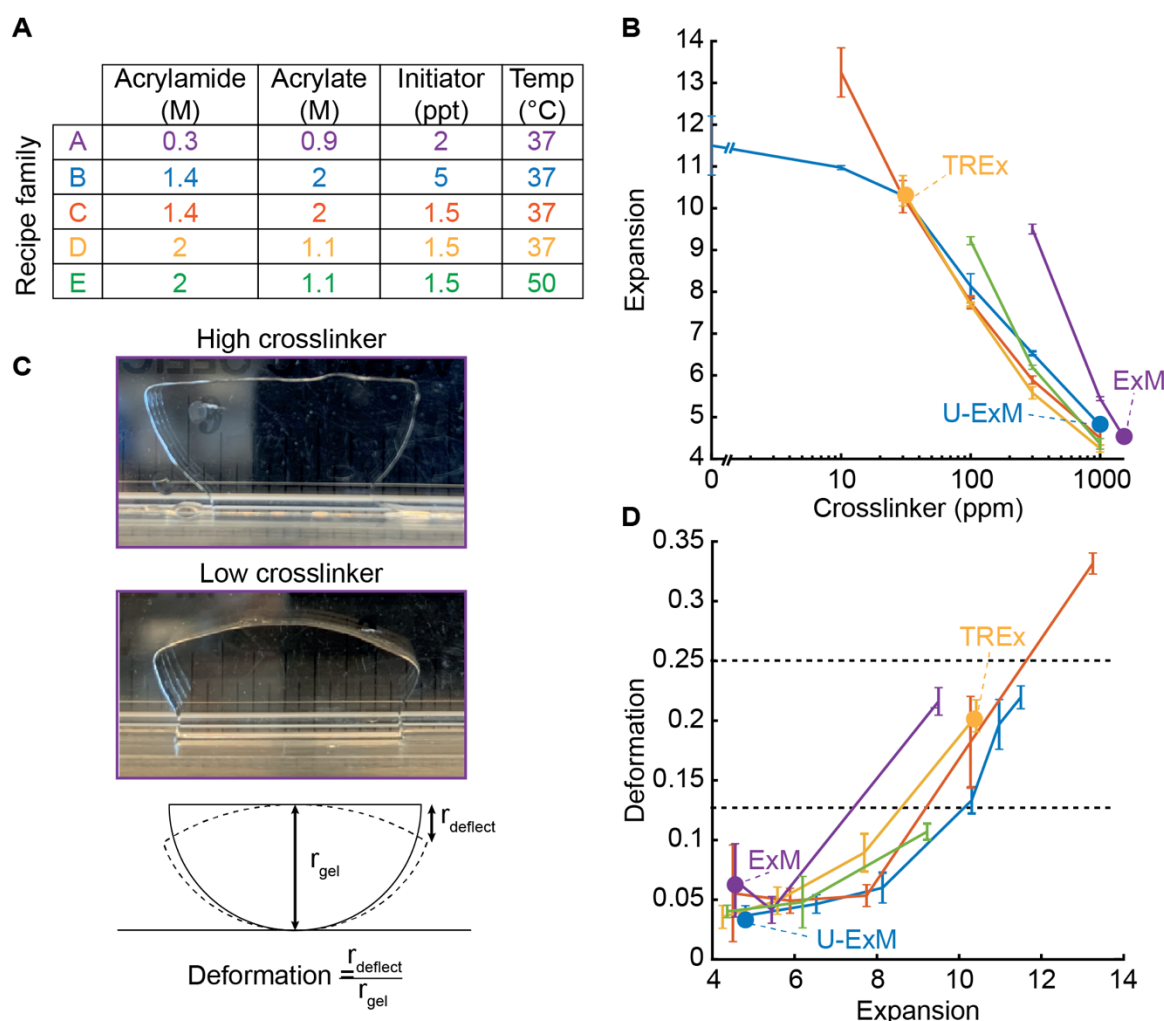
FIGURES

**FIGURE 1: Development of TREx gel recipe**

A) Parameters of gel recipe families explored, including component concentrations and gelation temperature. Each family was characterized by keeping these conditions constant while systematically varying the crosslinker concentration.

B) Expansion factor (mean ±s.d., n=3) versus crosslinker concentration (log scale) for each gel recipe family without biological specimens. Line colors correspond to recipe families as in 1A. Specific recipes (with specific crosslinker concentrations) are indicated as follows: filled purple dot - original ExM recipe, blue dot - UltraExM, and yellow dot - TREx. All recipe families were tested with crosslinker concentrations of 0, 10, 30, 100, 300, 1000 ppm, plus an addition condition with 1500 ppm for family A corresponding to the original ExM recipe. Only conditions in which gels formed are plotted.

21

569   C) Definition of gel deformation index. Example gels from recipe family A with high crosslinker and low

570   deformation (top panel, 1.5 ppt), and low crosslinker and high deformation (middle panel, 300 ppm).

571   Bottom panel, schematic illustrating deformation index measurement.

572   D) Deformation index (mean ±s.d., n=3) versus expansion factor for each gel recipe family without

573   biological specimens, with line colors and dots corresponding to specific recipes as in 1A and 1B.

574   Horizontal grey lines indicate thresholds for gels with mechanical quality deemed perfect (deformation <

575   0.125) and acceptable (deformation < 0.25). Ideal recipes would occupy the lower right quadrant,

576   corresponding to high expansion and low deformability.

577

22
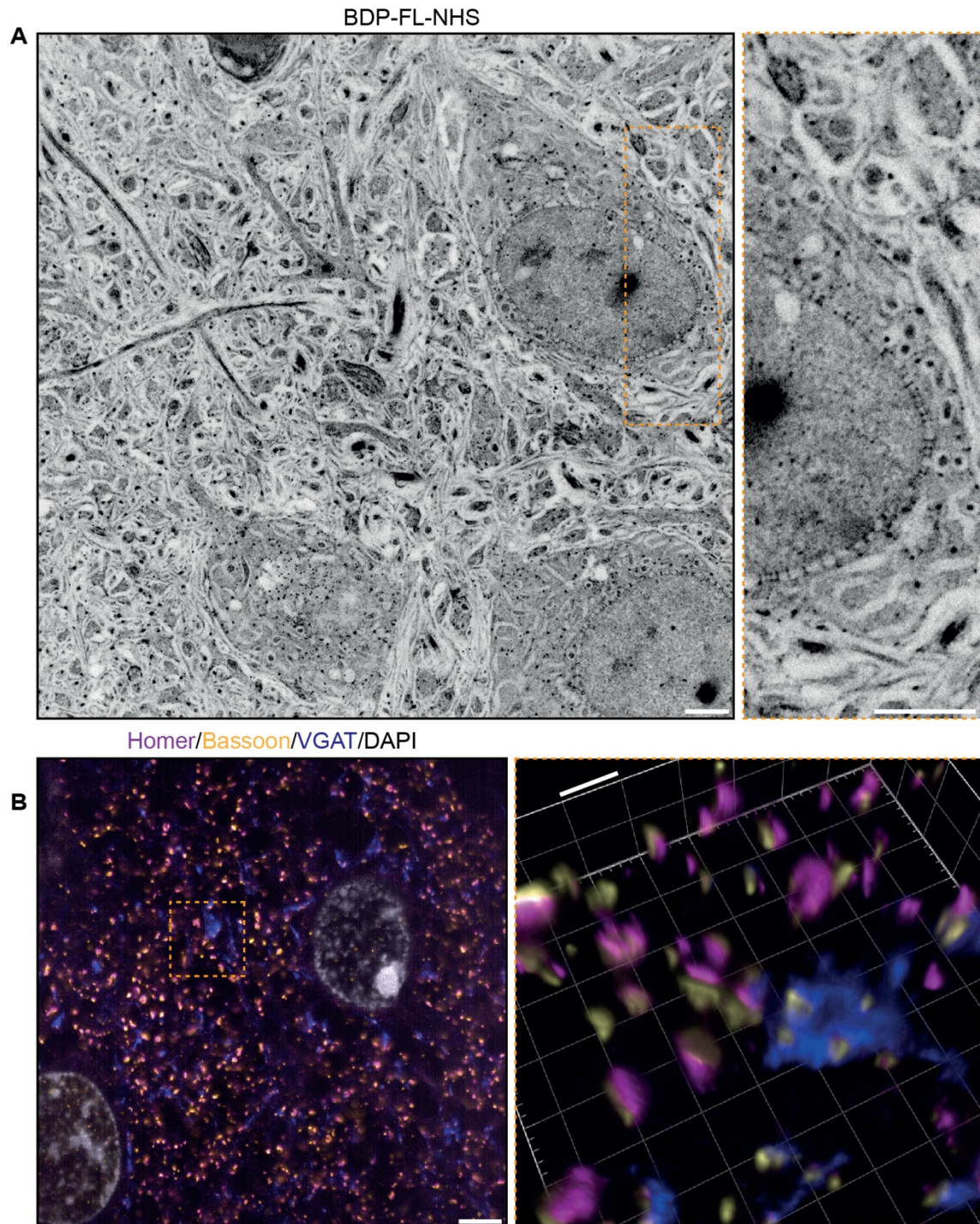
FIGURE 2: TREx in mouse brain tissue slices

A) Mouse brain tissue (cortex) expanded using TREx, stained for total protein content with BODPIY-FL NHS, and imaged by confocal microscopy. Displayed contrast is inverted to show dense stained regions as

23

582   dark. Inset, zoom-in showing nuclear envelope with densely stained structures spanning the nuclear

583   envelope, consistent with nuclear pore complexes.

584   B) Mouse brain tissue (cortex) stained with antibodies against (purple) homer, (yellow) bassoon, and (blue)

585   VGAT, and DAPI (grey), and expanded using TREx. Inset, zoom-in showing paired bassoon and homer-

586   rich structures, consistent with excitatory synapses and complex structured pre-synaptic vesicle pool

587   marked by VGAT bearing several release sites marked by bassoon.

588   Scale bars (corrected to indicate pre-expansion dimensions): main ~2 μm, zooms ~400 nm

589

590

24

591
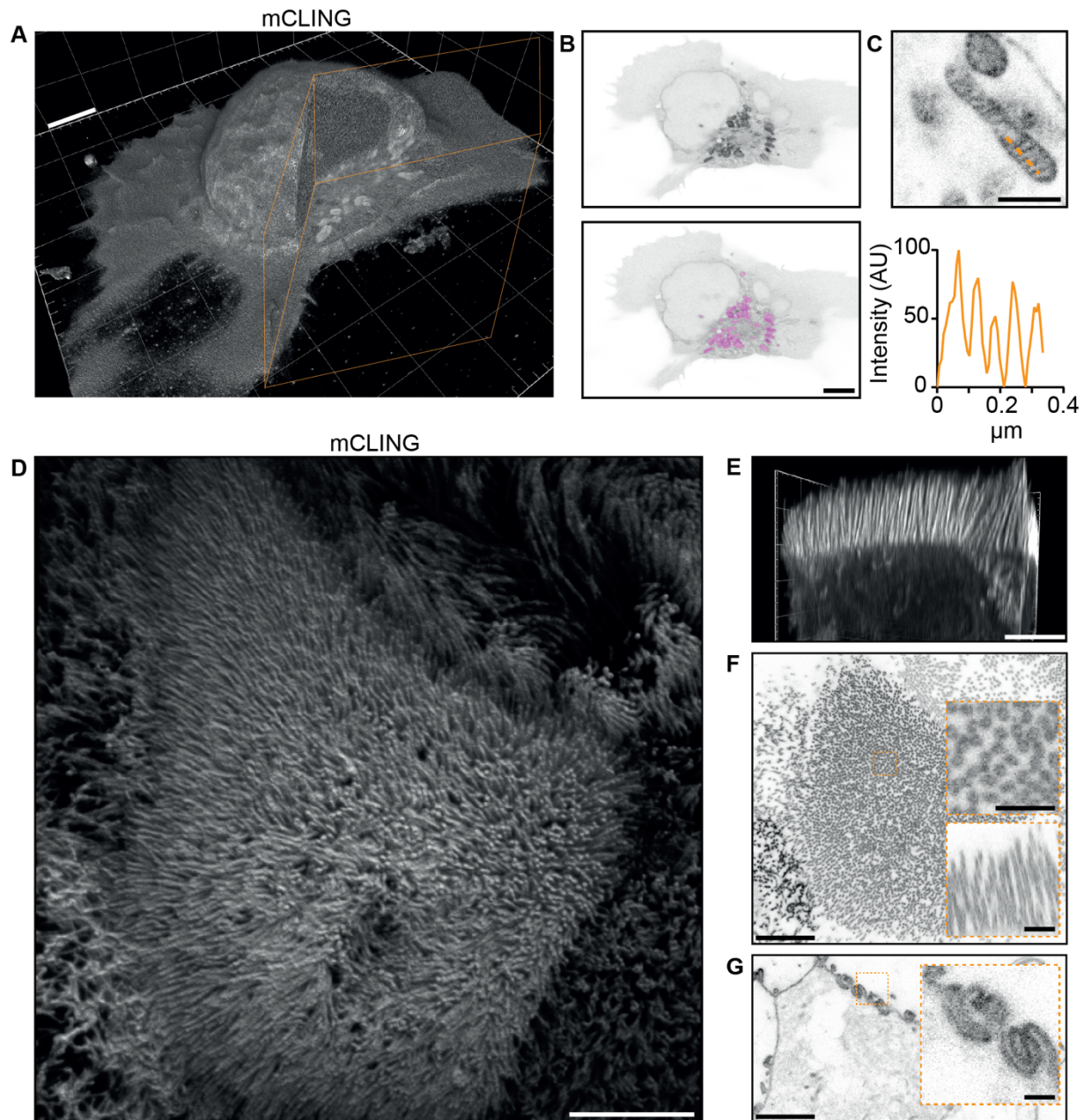
FIGURE 3: TREx can be used to visualize the ultrastructure of cellular membranes

A) Volumetric render of Jurkat T cell activated on anti-CD3 coated coverslip fixed and stained using mCLING. Colored clipping planes indicate portion clipped out to reveal intracellular detail.

B) Immunological synapse of activated T cell stained with mCLING in (A) revealing organelle clustering at the immunological synapse. Below: mitochondria segmented using the trainable Weka segmentation algorithm indicated in magenta.

25

598   C) Representative example of mitochondrion in T cells visualized with mCLING. Line profile along the

599   orange dashed line indicates mitochondrial cristae.

600   D) Volumetric projection of Caco2 monolayer apical brush border as seen from above looking down on the

601   cells.

602   E) Volumetric side projection of a portion of the cell shown in D as seen from the side.
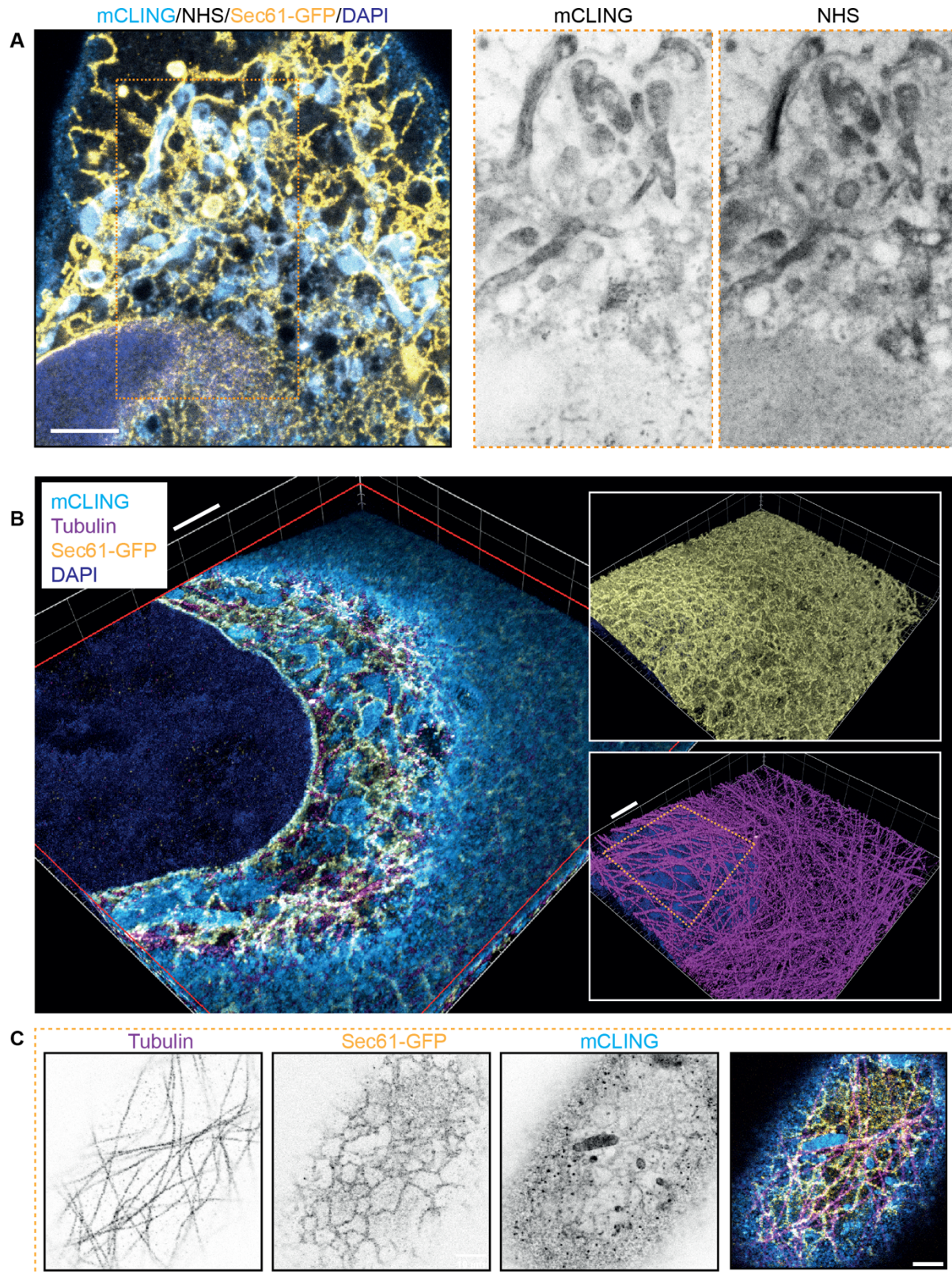
603   F) Brush border x, y plane of the cell shown in D, with zooms revealing hollow microvilli.

604   G) Similar to F, representative plane below the apical surface revealing highly interdigitated cell-cell

605   contacts.

606   Scale bars (corrected to indicate pre-expansion dimensions): A, B, D, E ~2 μm, C ~500 nm, F and G main

607   ~2 μm and zooms ~500 nm

608

609

FIGURE 4: TREx Microscopy can combine antibody-based staining with NHS ester total protein

27

611 **stain to provide cellular context**

612 A) Merged plane of expanded U2OS cell expressing GFP-Sec61β stained for mCLING, GFP, NHS ester

613 and DAPI. Single planes of mCLING and NHS ester are displayed in inverted contrast.

614 B) Volumetric render of U2OS cell expressing GFP-Sec61β Sec61β stained for mCLING, GFP and tubulin.

615 Top portion of cell is clipped with clipping plane indicated in red. Volumetric render of entire volume for

616 GFP and tubulin in insert A and B, respectively.

617 C) Single planes displayed in inverted contrast of the top of cell in B revealing the tight spatial organization.

618 Scale bars (corrected to indicate pre-expansion dimensions): A, C ~1 μm, B ~2 μm

619

620 **SUPPLEMENTAL MOVIES**

621 **Supplemental Movie 1:** Z-stack of Fig. 2A

622 **Supplemental Movie 2:** 3D render of Fig. 2B

623 **Supplemental Movie 3:** 3D render of Fig. 3A

624 **Supplemental Movie 4:** 3D render of Fig. 3D

625 **Supplemental Movie 5:** 3D render of Fig. 4B

28